

Simple Numerical Solutions to the Einstein Constraints on Various Three-Manifolds

Fan Zhang · Lee Lindblom*

October 27, 2022

Abstract Numerical solutions to the Einstein constraint equations are constructed on a selection of compact orientable three-dimensional manifolds with non-trivial topologies. A simple constant mean curvature solution and a somewhat more complicated non-constant mean curvature solution are computed on example manifolds from three of the eight Thursten geometrization classes. The constant mean curvature solutions found here are also solutions to the Yamabe problem that transforms a geometry into one with constant scalar curvature.

Keywords Einstein constraints, numerical solutions, numerical relativity, Yamabe problem

1 Introduction

Einstein's gravitational field equations are a complicated non-linear second-order system of partial differential equations for the components of the space-time metric. Like the electromagnetic field equations, Einstein's equations can be written as a system of evolution equations plus constraints that must be

F. Zhang
Gravitational Wave and Cosmology Laboratory, Department of Astronomy, Beijing Normal University, Beijing 100875, China
Advanced Institute of Natural Sciences, Beijing Normal University at Zhuhai 519087, China
E-mail: fnzhang@bnu.edu.cn

L. Lindblom (corresponding author)
Center for Astrophysics and Space Sciences, University of California at San Diego, USA
E-mail: llindblom@ucsd.edu

satisfied at each instant of time, i.e. on any spacelike surface in the spacetime. These constraint equations are typically written as systems of elliptic partial differential equations, which must be solved on an initial time slice before an evolution can proceed to determine the full spacetime geometry. A variety of methods have been developed for solving these equations on spacetimes of interest to the numerical relativity community, e.g. for neutron star and black hole binary systems (see e.g. [1,2,3,4,5]). This paper focuses on a basic problem that has not received much attention in the literature to date. Solutions to the constraints are explored here on compact orientable three-manifolds having a variety of different topologies.

Standard numerical relativity codes at this time are not able to solve problems on manifolds with non-trivial topologies. Methods have been developed recently, however, that provide a way to solve partial differential equations numerically, including the Einstein constraints, on a wide variety of three-manifolds with different topologies [6]. Those methods are used here to find simple numerical solutions to the Einstein constraints on four different manifolds: $S^2 \times S^1$, $G^2 \times S^1$, $L(8,3)$ and $SFS[S^2 : (2,1)(2,1)(2,-1)]$. (The names used for these manifolds are those used in [7].) The first two, $S^2 \times S^1$ and $G^2 \times S^1$, are simple fiber-bundle spaces with S^1 (the circle) fibers and base spaces S^2 (the two-sphere) or G^2 (the genus two two-manifold). The $L(8,3)$ manifold is an example of a lens space obtained from the three-sphere (S^3) by identifying points related by a discrete isometry. The $SFS[S^2 : (2,1)(2,1)(2,-1)]$ manifold is a Seifert fibred space constructed from the $S^2 \times S^1$ fiber bundle by excising neighborhoods of three fibers from this space and twisting the fibers in these neighborhoods before re-attaching to the S^2 base manifold.

Section 2 reviews and summarizes the particular forms of the constraint equations used in this study. Section 3 describes the simple constant mean curvature (CMC) solutions to the constraints found here on the example manifolds described above. Numerical solutions to this equation are found using the pseudo-spectral methods implemented in the SpEC code (developed originally by the Caltech/Cornell numerical relativity collaboration [2]). These CMC solutions are also non-trivial solutions to the Yamabe problem that constructs a constant scalar curvature geometry on the manifold [8]. Section 4 describes the numerically more challenging and somewhat more complicated non-constant mean curvature (or variable mean curvature VMC) solutions to the constraints on these manifolds. Section 5 summarizes the main results, and suggests areas where the methods described here might be improved.

2 The Einstein Constraints

This section gives a brief introduction to the form of the constraint equations used in this study. Consider a spacetime containing a three-dimensional spacelike surface with future-directed timelike unit normal n^α .¹ The components of

¹ Greek letters are used for spacetime indices, e.g. α, β, \dots , and Latin letters for spatial indices on a surface, e.g. a, b, c, \dots

the Einstein equations,

$$G_{\alpha\beta} n^\alpha n^\beta = 8\pi T_{\alpha\beta} n^\alpha n^\beta, \quad (2.1)$$

$$G_{a\beta} n^\beta = 8\pi T_{a\beta} n^\beta, \quad (2.2)$$

play the role of initial value constraints on this surface. When re-written in terms of the spatial metric g_{ab} and extrinsic curvature K_{ab} of this surface, these equations have the form,

$$G_{\alpha\beta} n^\alpha n^\beta = \frac{1}{2} (R - K_{ab} K^{ab} + K^2) = 8\pi T_{\alpha\beta} n^\alpha n^\beta, \quad (2.3)$$

$$G_{a\beta} n^\beta = \nabla^b K_{ba} - \nabla_a K = 8\pi T_{a\beta} n^\beta, \quad (2.4)$$

where R is the scalar curvature associated with the metric g_{ab} , ∇_a is the g_{ab} metric-compatible covariant derivative, and $K = g^{ab} K_{ab}$ on this surface.

The most general and most widely used method of solving these constraints re-expresses g_{ab} and K_{ab} in terms of ‘‘conformal’’ fields ϕ , \tilde{g}_{ab} , $\tilde{\tau}$, $\tilde{\sigma}_{ab}$ and \tilde{W}_a (for a review see [9]):

$$g_{ab} = \phi^4 \tilde{g}_{ab}, \quad (2.5)$$

$$K_{ab} = \phi^{-2} (\tilde{\sigma}_{ab} + \widetilde{LW}_{ab}) + \frac{1}{3} \phi^4 \tilde{g}_{ab} \tilde{\tau}, \quad (2.6)$$

where $\phi > 0$ is the conformal factor, \tilde{g}_{ab} is a positive definite metric, $\tilde{\sigma}_{ab}$ is trace-free and divergence-free (with respect to the \tilde{g}_{ab} metric-compatible covariant derivative $\tilde{\nabla}_a$), and $\tilde{\tau} = K$. The tensor \widetilde{LW}_{ab} is defined as the shear of \tilde{W}_a :

$$\widetilde{LW}_{ab} = \tilde{\nabla}_a \tilde{W}_b + \tilde{\nabla}_b \tilde{W}_a - \frac{2}{3} \tilde{g}_{ab} \tilde{\nabla}_c \tilde{W}^c. \quad (2.7)$$

The constraints, Eqs. (2.3) and (2.4), can be re-written as a system of equations for ϕ and \tilde{W}_a by using the following identities that relate the covariant derivative ∇_a and $\tilde{\nabla}_a$ (the covariant derivative compatible with the conformal metric \tilde{g}_{ab}):

$$\nabla^a \rho_{ab} = \phi^{-6} \tilde{\nabla}^a (\phi^2 \rho_{ab}), \quad (2.8)$$

$$R = \phi^{-4} \tilde{R} - 8\phi^{-5} \tilde{\nabla}^a \tilde{\nabla}_a \phi, \quad (2.9)$$

where ρ_{ab} is any trace-free symmetric tensor field, and \tilde{R} is the scalar curvature associated with \tilde{g}_{ab} . Using these identities Eqs. (2.3) and (2.4) can be written as,

$$\tilde{\nabla}^a \tilde{\nabla}_a \phi = \frac{1}{8} \phi \tilde{R} + \frac{1}{12} \phi^5 \tilde{\tau}^2 - \frac{1}{8} \phi^{-7} (\tilde{\sigma}_{ab} + \widetilde{LW}_{ab}) (\tilde{\sigma}^{ab} + \widetilde{LW}^{ab}) - 2\pi \phi^5 T_{\perp\perp}, \quad (2.10)$$

$$\tilde{\nabla}^b (\widetilde{LW}_{ba}) = \frac{2}{3} \phi^6 \tilde{\nabla}_a \tilde{\tau} + 8\pi \phi^6 T_{a\perp}, \quad (2.11)$$

where $T_{\perp\perp} = T_{\alpha\beta} n^\alpha n^\beta$ and $T_{a\perp} = T_{a\beta} n^\beta$. The stress-energy components $T_{\perp\perp}$ and $T_{a\perp}$ are determined by the physical properties of the matter in the space-time, while the conformal fields \tilde{g}_{ab} , $\tilde{\sigma}_{ab}$, $\tilde{\tau}$ can be chosen freely. Once these stress-energy and conformal fields are fixed, Eqs. (2.10) and (2.11) become a second-order system of elliptic equations for ϕ and \tilde{W}_a .

Differentiable structures were constructed numerically in [6] for a collection of forty different three-manifolds having representative topologies from five of the eight Thurston geometrization classes [10, 11]. The goal here is to construct simple solutions to Eqs. (2.10) and (2.11) numerically on a selection of those manifolds. The procedure introduced in [6] produces a C^1 reference metric \tilde{g}_{ab} on these manifolds. Those reference metrics are used to construct Jacobians and a covariant derivative that define what it means for tensor fields to be continuous and differentiable across the boundaries between coordinate patches. These reference metrics are also used here as the conformal metric that appears in Eqs. (2.10) and (2.11).

The symmetric trace-free divergence-free tensor $\tilde{\sigma}_{ab}$ is often associated with gravitational-wave degrees of freedom. The differentiable structures constructed in [6] for these example manifolds provide no structure from which a suitable $\tilde{\sigma}_{ab}$ could easily be constructed. Therefore for simplicity the solutions constructed here set $\tilde{\sigma}_{ab} = 0$.

Another common simplification used in the solution to the Einstein constraints is to set $\tilde{\nabla}_a \tilde{\tau} = 0$. In this case the topologies of the manifolds on which vacuum solutions exist, i.e. those with $T_{\perp\perp} = T_{\perp a} = 0$, are known to be limited [12]. To avoid this restriction, a very simple form of matter is introduced to allow solutions to exist for all the cases considered here. In particular a cosmological constant Λ is included, whose stress energy tensor is given by,

$$T_{\alpha\beta} = -\frac{\Lambda}{8\pi}\psi_{\alpha\beta}, \quad (2.12)$$

where $\psi_{\alpha\beta}$ is the full spacetime-metric. The components $T_{\perp\perp}$ and $T_{\perp a}$ that enter the constraints in this case, are given by,

$$T_{\perp\perp} = \frac{\Lambda}{8\pi}, \quad (2.13)$$

$$T_{\perp a} = 0. \quad (2.14)$$

These assumptions simplify the structures of Eqs. (2.10) and (2.11):

$$\tilde{\nabla}^a \tilde{\nabla}_a \phi = \frac{1}{8}\phi \tilde{R} + \frac{1}{12}\phi^5 (\tilde{\tau}^2 - 3\Lambda) - \frac{1}{8}\phi^{-7} \widetilde{LW}_{ab} \widetilde{LW}^{ab}, \quad (2.15)$$

$$\tilde{\nabla}^b (\widetilde{LW}_{ba}) = \frac{2}{3}\phi^6 \tilde{\nabla}_a \tilde{\tau}. \quad (2.16)$$

Two classes of simple solutions to these equations are constructed numerically in the following sections: those with $\tilde{\nabla}_a \tilde{\tau} = 0$ (the constant mean curvature solutions) in Sec. 3, and those with $\tilde{\nabla}_a \tilde{\tau} \neq 0$ (the variable mean curvature solutions) in Sec. 4.

An important way to measure how well the numerical solutions successfully solve Eqs. (2.15) and (2.16) is to evaluate how well they satisfy the original Einstein constraints Eqs. (2.3) and (2.4). To do that the physical metric g_{ab} and extrinsic curvature K_{ab} are re-constructed from the numerically determined ϕ and \tilde{W}_a using Eqs. (2.5) and (2.6). The scalar curvature R associated with g_{ab} is then determined numerically, which allows the original forms of the

Hamiltonian \mathcal{H} and momentum \mathcal{M}_a constraints, Eqs. (2.3) and (2.4), to be evaluated,

$$\mathcal{H} = R - K_{ab}K^{ab} + K^2 - 16\pi T_{\perp\perp}, \quad (2.17)$$

$$\mathcal{M}_a = \nabla^b K_{ba} - \nabla_a K - 8\pi T_{\perp a}. \quad (2.18)$$

The accuracy of the resulting g_{ab} and K_{ab} can then be measured using the following constraint norm,

$$\mathcal{C}^2 = \mathcal{V}^{-1} \int (\mathcal{H}^2 + g^{ab} \mathcal{M}_a \mathcal{M}_b) \sqrt{\det g} d^3x, \quad (2.19)$$

where \mathcal{V} is the proper volume of the manifold,

$$\mathcal{V} = \int \sqrt{\det g} d^3x. \quad (2.20)$$

This norm, \mathcal{C} , vanishes for an exact solution to the Einstein constraints, so a non-zero value is a useful measure of the accuracy of a numerical solution.

3 Simple Constant Mean Curvature (CMC) Solutions

This section defines a simple one parameter family of constant mean curvature (CMC) solutions to the Einstein constraints, and reports the results of numerical evaluations of these solutions on a selection of three-dimensional manifolds with different topologies.

In the constant mean curvature case, $\tilde{\nabla}_a \tilde{\tau} = 0$, the Einstein constraints Eqs. (2.15) and (2.16) simplify considerably. In particular Eq. (2.16) becomes a homogeneous elliptic equation for \tilde{W}_a , $\tilde{\nabla}^b (\tilde{L} \tilde{W}_{ab}) = 0$, whose simplest (and in most cases unique²) solution is $\tilde{W}_a = 0$. This in turn reduces Eq. (2.15) to the following,

$$\tilde{\nabla}^a \tilde{\nabla}_a \phi = \frac{1}{8} \phi \tilde{R} + \frac{1}{12} \phi^5 (\tilde{\tau}^2 - 3\Lambda). \quad (3.1)$$

The integral of the left side of Eq. (3.1) vanishes on any compact manifold. Therefore the constants $\tilde{\tau}$ and Λ must be chosen in a way that makes it possible for the integral of the right side of this equation to vanish as well. Convenient choices for these constants would produce solutions to Eq. (3.1) with $\phi \approx 1$. Such choices can be identified by setting $\phi = 1$ in the expression on the right side of Eq. (3.1) and integrating over the manifold. Setting this integral to zero results in the values,

$$\tilde{\tau}^2 - 3\Lambda = -\frac{3}{2} \langle \tilde{R} \rangle, \quad (3.2)$$

² The $W_a = 0$ solution is unique up to the addition of a conformal Killing field, and none exist for most geometries.

where $\langle \tilde{R} \rangle$ is the average value of the conformal scalar curvature \tilde{R} ,

$$\langle \tilde{R} \rangle = \frac{\int \sqrt{\det \tilde{g}} \tilde{R} d^3x}{\int \sqrt{\det \tilde{g}} d^3x}. \quad (3.3)$$

This choice transforms Eq. (3.1) into the form

$$\tilde{\nabla}^a \tilde{\nabla}_a \phi = \frac{1}{8} \phi \left(\tilde{R} - \phi^4 \langle \tilde{R} \rangle \right). \quad (3.4)$$

This equation has the exact solution $\phi = 1$ in the constant scalar curvature case $\tilde{R} = \langle \tilde{R} \rangle$, and admits solutions in all the CMC cases studied here. The integral of the right side of Eq. (3.1) must vanish for any solution ϕ . If $\phi > 0$ and $\tilde{R} > 0$ this integral can vanish only if $\tilde{\tau}^2 - 3\Lambda < 0$. Thus no $\phi > 0$ solution can exist to Eq. (3.1) when $\tilde{R} > 0$ unless the cosmological constant satisfies the inequality, $\Lambda > \frac{1}{3}\tilde{\tau}^2 \geq 0$.

Once a conformal metric \tilde{g}_{ab} is chosen, Eq. (3.4) becomes a second-order elliptic differential equation that can be solved using a variety of standard numerical methods. The conformal metrics used for the examples in this study are the reference metrics constructed in [6] for building differentiable structures on these manifolds. These positive-definite metrics are smooth within each cubic coordinate chart, and are continuous and differentiable in the appropriate senses across the interfaces between charts.

Table 3.1 lists the compact orientable manifolds selected for this study, $S^2 \times S^1$, $G^2 \times S^1$, $L(8, 3)$ and $SFS[S^2 : (2, 1)(2, 1)(2, -1)]$, which are described in physical terms briefly in Sec. 1. These three-manifolds belong to three different Thurston geometrization classes: $L(8, 3)$ and $SFS[S^2 : (2, 1)(2, 1)(2, -1)]$ belong to the S^3 class, $G^2 \times S^1$ belongs to the $H^2 \times S^1$ class, and $S^2 \times S^1$ is the defining member of the $S^2 \times S^1$ class. This table also lists $\langle \tilde{R} \rangle$ defined in Eq. (3.3) and the physical volumes $\mathcal{V}(\text{CMC})$ defined in Eq. (2.20) for the CMC geometries constructed in this study on each of these manifolds. These volumes measure the physical ‘‘sizes’’ of the manifolds in the length-scale units of our code, and can therefore be used to calibrate the sizes of the curvatures of the geometries.

Table 3.1: Compact orientable manifolds included in this study. Also listed are the average scalar curvature $\langle \tilde{R} \rangle$ defined in Eq. (3.3), and the physical volumes $\mathcal{V}(\text{CMC})$ defined in Eq. (2.20) for the CMC geometries constructed on each manifold.

Manifold	$\langle \tilde{R} \rangle$	$\mathcal{V}(\text{CMC})$
$G^2 \times S^1$	-2.97	9.68
$L(8, 3)$	2.66	8.23
$S^2 \times S^1$	2.69	9.42
$SFS[S^2 : (2, 1)(2, 1)(2, -1)]$	2.66	8.23

Numerical solutions of Eq. (3.4) are constructed in this study using multicube representations of these manifolds, as described in [6, 13]. A multicube

representation is a collection of non-overlapping cubes in \mathbb{R}^3 together with maps that specify how the faces are identified with the faces of neighboring cubes. These multicube regions serve as the coordinate charts used to represent tensor fields on these manifolds. Complete descriptions of the multicube structures used for each of the manifolds included in this study are included in Appendix A. Figure 3.1 illustrates the multicube structure used to represent the $G2 \times S1$ manifold, with surface colors representing $\sqrt{\det \tilde{g}}$ and \tilde{R} for the reference metric used here. Blue colors in these figures represent small values of these scalars, and red colors represent large values. The scalar curvatures \tilde{R} for the reference metrics used in this study are not constant, as illustrated in Fig. 3.1b. Therefore the constraint Eq. (3.4) is not trivial even in the simple CMC case studied here.

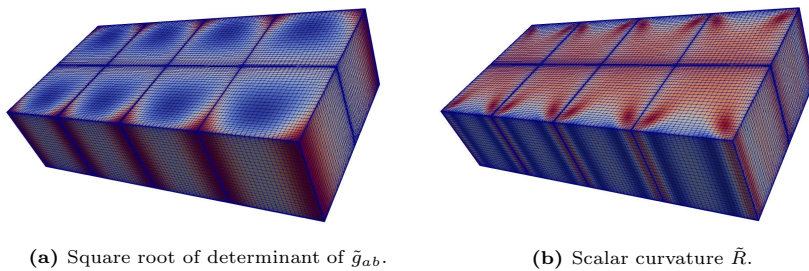


Fig. 3.1: Views of the multicube structure used to represent the $G2 \times S1$ manifold, along with the surface values of the determinant of the reference metric, $\sqrt{\det \tilde{g}}$, and the scalar curvature \tilde{R} .

For this study the differential Eq. (3.4) has been solved numerically using the pseudo-spectral methods implemented in the SpEC numerical relativity code [2]. Functions are represented by their values on a grid defined by the locations of the Gauss-Lobatto collocation points. Representing functions in this way provides a numerically efficient way to transform back and forth between the grid representation of functions, and their representation as Chebyshev polynomial expansions. Derivatives are evaluated numerically using the exact analytic expressions for the derivatives of those Chebyshev expansions. The elliptic differential operator in Eq. (3.4) becomes in effect a linear matrix that operates on the vector of grid values of ϕ . Boundary conditions are included in this matrix operator by replacing the equation for the elliptic operator by equations that enforce the continuity of ϕ and its gradient $\nabla\phi$ on the grid points along the interface boundaries between the multicube coordinate charts. Details about how the SpEC code implements these boundary conditions can be found in [2] and more specifically for multicube manifolds in Sec. 5 of [13]. The non-linear Eq. (3.4) is solved in effect by minimizing the discrete version

of the residual \mathcal{E} defined by

$$\mathcal{E} = \tilde{\nabla}^a \tilde{\nabla}_a \phi - \frac{1}{8} \phi \left(\tilde{R} - \phi^4 \langle \tilde{R} \rangle \right). \quad (3.5)$$

The SpEC code minimizes these residuals by accessing the ksp linear solver and the snes non-linear solver from the PETSC software library [14]. These solves are done iteratively, starting with the initial guess $\phi = 1$ for the lowest spatial resolution. Once the solver finds a solution that satisfactorily minimizes \mathcal{E} for one resolution, that solution is interpolated onto the next higher resolution grid as its initial guess. This procedure is repeated through a series of increasing numerical resolutions. Solving the equation in this way mimics the advantages of a multi-grid solver by allowing the long length-scale features of the solution (which take the longest to converge numerically) to be determined in the faster low-resolution solves. The CMC solutions for this study have been computed on a sequence of grids with $N = \{16, 20, 24, 28, 32, 35\}$ collocation points in each spatial direction in each multicube region. The SpEC code parallelizes these computations (up to a point) by allowing each multicube region to be run on a separate processor. These numerical computations take a very long time, and this has limited our ability to consider additional example manifolds or to explore them with higher numerical resolutions.

The constraint norm \mathcal{C} defined in Eq. (2.19) vanishes for any exact solution to the constraint equations and is therefore an important and useful measure of the accuracy of the numerical solutions. This constraint norm has a particularly simple form for these simple CMC solutions. The momentum constraint from Eq. (2.18) is satisfied identically in this case, $\mathcal{M}_a = 0$, since $\tilde{\sigma}_{ab} = \tilde{W}_a = 0$. Thus \mathcal{C} depends only on the Hamiltonian constraint \mathcal{H} defined in Eq. (2.17). For the CMC case \mathcal{H} is given by

$$\mathcal{H} = R + \frac{2}{3} (\tilde{\tau}^2 - 3\Lambda) = R - \langle \tilde{R} \rangle. \quad (3.6)$$

Consequently the constraint norm \mathcal{C} becomes

$$\mathcal{C}^2 = \nu^{-1} \int \left(R - \langle \tilde{R} \rangle \right)^2 \sqrt{\det g} d^3x. \quad (3.7)$$

The vanishing of \mathcal{C} implies that the scalar curvature R is constant, $R = \langle \tilde{R} \rangle$, for these simple CMC solutions. Thus the conformal factor ϕ is the solution to the Yamabe problem that transforms \tilde{g}_{ab} into the constant scalar curvature metric g_{ab} [8]. Figure 3.2 illustrates the values of the constraint \mathcal{C} as a function of the spatial resolution N (the number of grid points in each direction of each multicube region) for each of the manifolds studied here. These results show that our numerical methods (generally) converge with increasing values of the spatial resolution N , and produce reasonably accurate solutions to the constraint equations. The values of \mathcal{C} for the $N = 35$ resolutions of the $G2 \times S1$ and $S2 \times S1$ manifolds are larger than expected. These numerical solutions are very time consuming for the higher resolution cases, and it is possible that the final results reported here could have been improved somewhat with more

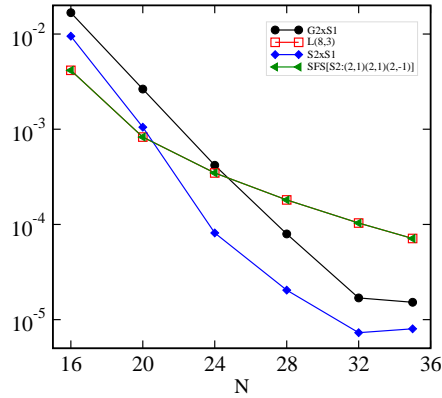


Fig. 3.2: Norm of the Einstein constraints, \mathcal{C} , as functions of the numerical resolution N for the numerical CMC initial data solutions.

computer time or perhaps by setting somewhat different parameters in the PETSC solvers.

Solutions to the CMC Einstein constraint Eq. (3.4) should be smooth across the interface boundaries between multicube coordinate patches. Therefore the continuity of the resulting solutions and their derivatives across those interface boundaries is another basic measure of how well these numerical solutions successfully solve the constraint equations globally. The L_2 norms of the differences between these boundary values of the conformal factor ϕ are computed by taking the square root of the squares of the differences averaged over all the boundary grid points. These norms are shown in Fig. 3.3 for each numerical resolution N for each of the manifolds studied here. The results show that the numerical CMC solutions have boundary continuity errors that are orders of magnitude smaller than the Einstein constraint errors for these solutions shown in Fig. 3.2. These discontinuity errors therefore do not contribute significantly to the Einstein constraint errors for these solutions.

4 Simple Variable Mean Curvature (VMC) Solutions

This section defines a simple one parameter family of variable mean curvature (VMC) solutions to the Einstein constraints, and reports the results of numerical evaluations of these solutions on a selection of three-dimensional manifolds with different topologies.

The constraint equations in the simple VMC case studied here are given by,

$$\tilde{\nabla}^a \tilde{\nabla}_a \phi = \frac{1}{8} \phi \tilde{R} + \frac{1}{12} \phi^5 (\tilde{\tau}^2 - 3\Lambda) - \frac{1}{8} \phi^{-7} \widetilde{LW}_{ab} \widetilde{LW}^{ab}, \quad (4.1)$$

$$\tilde{\nabla}^b (\widetilde{LW}_{ba}) = \frac{2}{3} \phi^6 \tilde{\nabla}_a \tilde{\tau}. \quad (4.2)$$

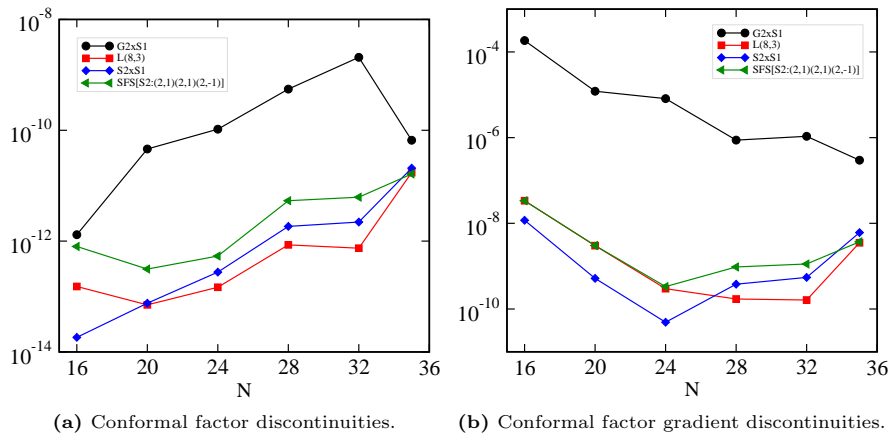


Fig. 3.3: Norms of the interface discontinuities in the conformal factor and its gradient as functions of the spatial resolution N for the CMC solutions.

These become a second-order system of elliptic equations for ϕ and \tilde{W}_a once the conformal fields \tilde{g}_{ab} , $\tilde{\sigma}_{ab}$, $\tilde{\tau}$ and the cosmological constant Λ are chosen. Unlike the CMC case, these equations are coupled so they must be solved as a single large system rather than individually one after the other.

The conformal fields \tilde{g}_{ab} and $\tilde{\sigma}_{ab}$ for these simple VMC solutions are chosen to be the same as those used for the CMC solutions described in Sec. 3. The conformal metric \tilde{g}_{ab} is identified with the reference metric constructed using the methods describe in [6] for that manifold. The transverse trace-free part of the conformal extrinsic curvature, $\tilde{\sigma}_{ab}$ is set to zero. Given these choices, the only remaining freedoms are the choices of a suitable non-constant $\tilde{\tau}$ and the cosmological constant Λ .

The only requirements on $\tilde{\tau}$ are that it must be continuous and differentiable, even across the interfaces between multicube regions, and sufficiently slowly varying to be easily resolved by the numerical code. One possibility is to set

$$\tilde{\tau} = A \left(1 + B h(s^x) h(s^y) h(s^z) \right), \quad (4.3)$$

where A and B are constants, s^x , s^y and s^z are re-scaled local coordinates in each multicube coordinate chart with ranges $-1 \leq s^x, s^y, s^z \leq 1$, and $h(s)$ is defined by

$$h(s) = \frac{8}{15} - (1 - s^2)^2. \quad (4.4)$$

This $h(s)$ has the value $h(\pm 1) = \frac{8}{15}$ and derivative $\frac{dh(\pm 1)}{ds} = 0$ on each of the boundaries of the coordinate patch where $s^2 = 1$. (The $\frac{8}{15}$ constant was chosen to make the integral of $h(s)$ vanish.) Therefore $\tilde{\tau}$ defined in Eq. (4.3) is continuous and differentiable in the appropriate sense for any values of the global constants A and B . The spatial average of $\tilde{\tau}$ is $\langle \tilde{\tau} \rangle = A$, so a natural choice for A is $A^2 = |\langle \tilde{R} \rangle|$, which makes the scale of the extrinsic curvature

comparable to the scale of the scalar curvature \tilde{R} . The spatial variation in $\tilde{\tau}$ is determined by B . The variance μ is defined as the rms average spatial variation in $\tilde{\tau}$, and is related to B by $B^2 = \mu^2 \left(\frac{525}{64}\right)^3$. Using these choices for A and B produces the $\tilde{\tau}$ used here for the simple VMC solutions:

$$\tilde{\tau} = |\langle \tilde{R} \rangle|^{1/2} \left[1 + \mu \left(\frac{525}{64}\right)^{3/2} h(s^x)h(s^y)h(s^z) \right]. \quad (4.5)$$

Figure 4.1 illustrates the surface values of this $\tilde{\tau}$ on the multicube structure used to represent the $G2 \times S1$ manifold in this study. The variance parameter $\mu = 0.1$ used for the example in this figure results in spatial variations of $\tilde{\tau}$ with $\max \tilde{\tau} / \min \tilde{\tau} \approx 1.8$.

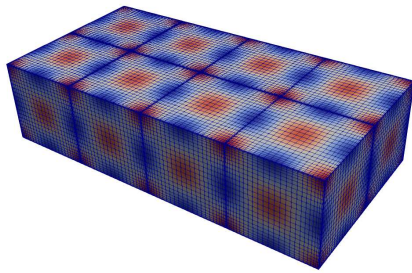


Fig. 4.1: Surface values of $\tilde{\tau}$ for the simple VMC solution on the $G2 \times S1$ manifold. The scale of the spatial variations in $\tilde{\tau}$ is set by the variance parameter μ . In the example shown here $\mu = 0.1$ which has $\max \tilde{\tau} / \min \tilde{\tau} \approx 1.8$.

The last choice needed to fix these simple VMC solutions is the value of the cosmological constant Λ . If a solution to Eq. (4.1) exists, the integral of its right side must vanish. The idea is to choose Λ that makes it possible to have solutions with $\phi \approx 1$. In this case the spatial average of the terms on the right side of Eq. (4.1) must satisfy,

$$0 \approx \frac{1}{8} \langle \tilde{R} \rangle - \frac{1}{8} \langle \widetilde{LW}_{ab} \widetilde{LW}^{ab} \rangle + \frac{1}{12} \langle \tilde{\tau}^2 \rangle - \frac{1}{4} \Lambda. \quad (4.6)$$

From Eq. (4.2) it follows that the spatial variations in \widetilde{LW}_{ab} should be comparable in size to the spatial variations in $\tilde{\tau}$, i.e. $\langle \widetilde{LW}_{ab} \widetilde{LW}^{ab} \rangle \approx \frac{4}{9} \mu^2 \langle \tilde{\tau} \rangle^2$. The quantity $\langle \tilde{\tau}^2 \rangle$ that appears in Eq. 4.6 is also determined by the spatial variation in $\tilde{\tau}$: $\langle \tilde{\tau}^2 \rangle = (1 + \mu^2) \langle \tilde{\tau} \rangle^2$. Thus a suitable choice for Λ should be

$$\Lambda = \frac{1}{2} \langle \tilde{R} \rangle + \frac{1}{9} (3 + \mu^2) |\langle \tilde{R} \rangle|. \quad (4.7)$$

The simple VMC solutions described above were constructed in this study by solving Eqs. (4.1) and (4.2) numerically. These solutions were obtained for each of the manifolds listed in Table 4.1 using the numerical methods described

in Sec. 3 for the CMC case. The expression used for $\tilde{\tau}$ in these solutions is given in Eq. (4.5). The variance parameter in this expression is set to $\mu = 0.1$ for the solutions on the $G2 \times S1$ and the $S2 \times S1$ manifolds, and $\mu = 0.01$ for the $L(8, 3)$ and $SFS[S2 : (2, 1)(2, 1)(2, -1)]$ manifolds to speed up convergence in those cases. The cosmological constant Λ used for these simple VMC solutions is given in Eq. (4.7).

Table 4.1: Physical volumes $\mathcal{V}(\text{VMC})$ defined in Eq. (2.20) for the VMC geometries constructed on the manifolds in this study. Also listed are the average scalar curvature $\langle \tilde{R} \rangle$ defined in Eq. (3.3) for each manifold.

Manifold	$\langle \tilde{R} \rangle$	$\mathcal{V}(\text{VMC})$
$G2 \times S1$	-2.97	8.20
$L(8, 3)$	2.66	8.23
$S2 \times S1$	2.69	9.39
$SFS[S2 : (2, 1)(2, 1)(2, -1)]$	2.66	8.23

The VMC Eqs. (4.1) and (4.2) are a much more complicated system than the simple scalar CMC Eq. (3.1). Consequently the numerical convergence is significantly slower. This inefficiency made it impractical to consider solutions with numerical resolutions larger than $N = 28$ for this study. The $N \leq 28$ solutions took several months running in parallel (one processor for each cubic region) to achieve a satisfactory level of convergence. Figure 4.2 shows the norm of the Einstein constraints Eq. (2.19) for these numerical VMC solutions, which are similar in size to the CMC constraint norms at the same resolutions in Fig. 3.2. Figure 4.3 shows the norms of the discontinuities in the conformal factor and its gradient across the boundary interfaces between the multicube regions. The sizes of these discontinuities are also comparable to those for the CMC solutions at the same numerical resolutions in Fig. 3.3.

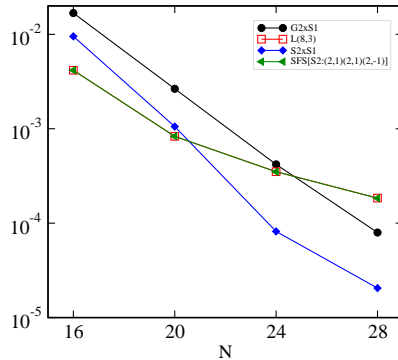


Fig. 4.2: Norm of the Einstein constraints, \mathcal{C} , for the numerical VMC initial data solutions.

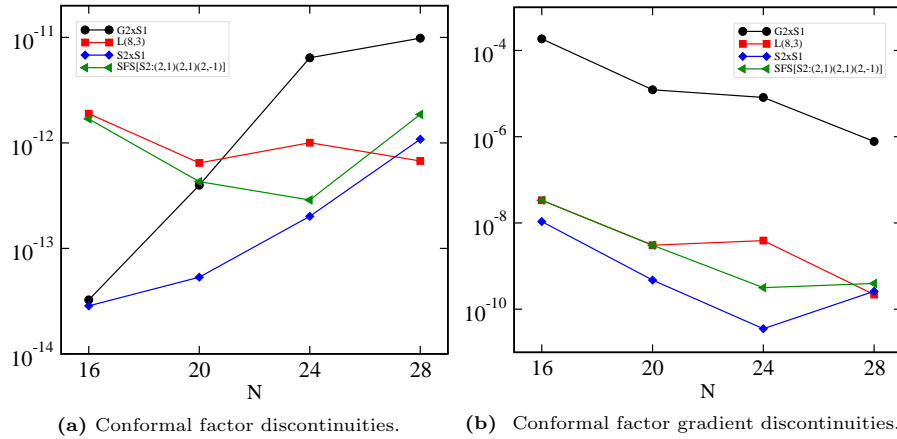


Fig. 4.3: Norms of the interface discontinuities in the conformal factor and its gradient as a function of spatial resolution N for the numerical VMC solutions.

5 Discussion

This paper outlines a basic framework for finding numerical solutions to the Einstein constraint equations on manifolds with non-trivial topologies. These ideas are illustrated here using simple constant mean curvature and variable mean curvature numerical solutions on several different compact orientable manifolds. The constant mean curvature solutions found here have constant scalar curvatures and are therefore solutions to the Yamabe problem on these manifolds as well. The one feature of these numerical examples that was surprising (to us) was the extreme inefficiency of our numerical elliptic solver. Some of the numerical VMC solutions presented here required running for months in parallel on a reasonably fast multiprocessor computer. We plan to study ways to improve this efficiency in a future project so that more cosmologically interesting solutions can be obtained and studied on a larger collection of manifolds. We plan to explore a variety of ways this might be done, e.g. through more efficient utilization of the PETSC solvers, by finding and implementing more efficient numerical methods for solving elliptic equations than those available in the SpEC code, or by finding different formulations of the Einstein constraints that can be solved numerically more efficiently.

A Appendix: Multicube Structures

A multicube structure consists of a set of non-overlapping cubes, \mathcal{B}_A , that cover the manifold, and a set of maps $\Psi_{B\beta}^{A\alpha}$ that identify the faces of neighboring cubes. The interface boundary maps used here (written in terms of the global Cartesian coordinates used for the multicube structure) take points, x_B^i , on the interface boundary $\partial_\beta \mathcal{B}_B$ of region \mathcal{B}_B to the

corresponding points, x_A^i , in the boundary $\partial_\alpha \mathcal{B}_A$ of region \mathcal{B}_A in the following way,

$$x_A^i = c_A^i + f_\alpha^i + C_{B\beta}^{A\alpha i} (x_B^j - c_B^j - f_\beta^j). \quad (\text{A.1})$$

The vectors $\vec{c}_A + \vec{f}_\alpha$ and $\vec{c}_B + \vec{f}_\beta$ are the locations of the centers of the $\partial_\alpha \mathcal{B}_A$ and $\partial_\beta \mathcal{B}_B$ faces respectively, and $\mathbf{C}_{B\beta}^{A\alpha}$ is the combined rotation/reflection matrix needed to orient the faces properly.

The multicube structures for two of the manifolds included in this study, $L(8,3)$ and $SFS[S2 : (2,1)(2,1)(2,-1)]$, were derived using the methods described in [6] from the triangulations of these manifolds given in the Regina catalog of compact orientable three-manifolds [7]. The multicube structure for $L(8,3)$ is given here in Table A.1. The multicube structure for $SFS[S2 : (2,1)(2,1)(2,-1)]$ was published previously in Table D.8 in [6], so it is not reproduced here. The multicube structures for the other two manifolds included in this study, $S2 \times S1$ and $G2 \times S1$ where constructed by hand. The multicube structure for $S2 \times S1$ was published previously in Table A.3 in [13]. The multicube structure used here for $G2 \times S1$ is based on the eight-region representation of the two-manifold $G2$ in Appendix B.5 in [15]. The resulting three-dimensional multicube structure is given here in Table A.2.

The following tables include lists of the cubic regions, \mathcal{B}_A , used to cover the manifold in each structure, the vectors \vec{c}_A that define the locations of the centers of these regions in \mathbb{R}^3 , and the rotation/reflection matrices $\mathbf{C}_{B\beta}^{A\alpha}$ needed to transform each cube face into the face of its neighbor.³ The identification of the $\partial_\beta \mathcal{B}_B$ face with the $\partial_\alpha \mathcal{B}_A$ face is indicated in the tables by $\{\alpha A\} \leftrightarrow \{\beta B\}$. The notation \mathbf{I} in these tables indicates the identity matrix, while \mathbf{R}_α indicates the $+\pi/2$ rotation about the outward directed normal to the $\{\alpha\}$ cube face.

Table A.1: Multicube representation of the Regina triangulation of the manifold $L(8,3)$. Multicube Structure: region center locations \vec{c}_A , region face identifications, $\{\alpha A\} \leftrightarrow \{\beta B\}$, and the rotation matrices for the associated interface maps, $\mathbf{C}_{A\alpha}^{B\beta}$.

A	\vec{c}_A	$\alpha = -x$ $B \beta \mathbf{C}_{A\alpha}^{B\beta}$	$\alpha = +x$ $B \beta \mathbf{C}_{A\alpha}^{B\beta}$	$\alpha = -y$ $B \beta \mathbf{C}_{A\alpha}^{B\beta}$
0.0	(0, 0, 0)	$0.3 + z \mathbf{R}_{-y} \mathbf{R}_{-x}$	$0.1 - x \mathbf{I}$	$1.2 + y \mathbf{I}$
0.1	(L , 0, 0)	$0.0 + x \mathbf{I}$	$0.2 - x \mathbf{R}_{+x}$	$1.1 + x \mathbf{R}_{-z}$
0.2	(0, L , 0)	$0.1 + x \mathbf{R}_{-x}$	$0.1 + y \mathbf{R}_{-z}$	$0.0 + y \mathbf{I}$
0.3	(0, 0, L)	$0.2 + y \mathbf{R}_{+x}^2 \mathbf{R}_{-z}$	$0.1 + z \mathbf{R}_{+y}$	$1.3 + z \mathbf{R}_{+x}$
1.0	($3L$, 0, 0)	$0.0 - z \mathbf{R}_{+y}$	$1.1 - x \mathbf{I}$	$1.1 - z \mathbf{R}_{-x} \mathbf{R}_{-y}$
1.1	($4L$, 0, 0)	$1.0 + x \mathbf{I}$	$0.1 - y \mathbf{R}_{+z}$	$1.2 - z \mathbf{R}_{+y}^2 \mathbf{R}_{+x}$
1.2	($3L$, L , 0)	$0.2 - z \mathbf{R}_{+y}$	$1.1 + y \mathbf{R}_{-z}$	$1.0 + y \mathbf{I}$
1.3	($3L$, 0, L)	$0.1 - z \mathbf{R}_{+y}$	$1.1 + z \mathbf{R}_{+y}$	$1.0 - z \mathbf{R}_{-x} \mathbf{R}_{-y}$

A	\vec{c}_A	$\alpha = +y$ $B \beta \mathbf{C}_{A\alpha}^{B\beta}$	$\alpha = -z$ $B \beta \mathbf{C}_{A\alpha}^{B\beta}$	$\alpha = +z$ $B \beta \mathbf{C}_{A\alpha}^{B\beta}$
0.0	(0, 0, 0)	$0.2 - y \mathbf{I}$	$1.0 - x \mathbf{R}_{-y}$	$0.3 - z \mathbf{I}$
0.1	(L , 0, 0)	$0.2 + x \mathbf{R}_{+z}$	$1.3 - x \mathbf{R}_{-y}$	$0.3 + x \mathbf{R}_{-y}$
0.2	(0, L , 0)	$0.3 - x \mathbf{R}_{+y}^2 \mathbf{R}_{+z}$	$1.2 - x \mathbf{R}_{-y}$	$0.3 + y \mathbf{R}_{+x}$
0.3	(0, 0, L)	$0.2 + z \mathbf{R}_{-x}$	$0.0 + z \mathbf{I}$	$0.0 - x \mathbf{R}_{+y} \mathbf{R}_{+z}$
1.0	($3L$, 0, 0)	$1.2 - y \mathbf{I}$	$1.3 - y \mathbf{R}_{+x} \mathbf{R}_{-z}$	$1.3 - z \mathbf{I}$
1.1	($4L$, 0, 0)	$1.2 + x \mathbf{R}_{+z}$	$1.0 - y \mathbf{R}_{+x} \mathbf{R}_{-z}$	$1.3 + x \mathbf{R}_{-y}$
1.2	($3L$, L , 0)	$0.0 - y \mathbf{I}$	$1.1 - y \mathbf{R}_{+z}^2 \mathbf{R}_{-x}$	$1.3 + y \mathbf{R}_{+x}$
1.3	($3L$, 0, L)	$1.2 + z \mathbf{R}_{-x}$	$1.0 + z \mathbf{I}$	$0.3 - y \mathbf{R}_{-x}$

³ The vectors \vec{f}_α are the relative positions of the center of the $A\{\alpha\}$ cube face with the center of region \mathcal{B}_A . These vectors are the same for all the cubic regions, and are given explicitly in [13] so they are not repeated here.

Table A.2: Multicube representation of the product space $G2 \times S1$ constructed from the genus number $N_g = 2$ two-dimensional compact orientable manifold. Multicube Structure: region center locations \vec{c}_A , region face identifications, $\{\alpha A\} \leftrightarrow \{\beta B\}$, and the rotation matrices for the associated interface maps, $\mathbf{C}_{A\alpha}^{B\beta}$.

A	\vec{c}_A	$\alpha = -x$ $B \beta \mathbf{C}_{A\alpha}^{B\beta}$	$\alpha = +x$ $B \beta \mathbf{C}_{A\alpha}^{B\beta}$	$\alpha = -y$ $B \beta \mathbf{C}_{A\alpha}^{B\beta}$	$\alpha = +y$ $B \beta \mathbf{C}_{A\alpha}^{B\beta}$	$\alpha = -z$ $B \beta \mathbf{C}_{A\alpha}^{B\beta}$	$\alpha = +z$ $B \beta \mathbf{C}_{A\alpha}^{B\beta}$
1	$(L, 2L, 0)$	$8 + x \mathbf{I}$	$8 - x \mathbf{I}$	$2 + y \mathbf{I}$	$4 - y \mathbf{I}$	$1 + z \mathbf{I}$	$1 - z \mathbf{I}$
2	$(L, L, 0)$	$7 + x \mathbf{I}$	$4 + x \mathbf{R}_{+z}^2$	$3 + y \mathbf{I}$	$1 - y \mathbf{I}$	$2 + z \mathbf{I}$	$2 - z \mathbf{I}$
3	$(L, 0, 0)$	$6 + x \mathbf{I}$	$6 - x \mathbf{I}$	$4 + y \mathbf{I}$	$2 - y \mathbf{I}$	$3 + z \mathbf{I}$	$3 - z \mathbf{I}$
4	$(L, -L, 0)$	$5 + x \mathbf{I}$	$2 + x \mathbf{R}_{-z}^2$	$1 + y \mathbf{I}$	$3 - y \mathbf{I}$	$4 + z \mathbf{I}$	$4 - z \mathbf{I}$
5	$(0, -L, 0)$	$7 - x \mathbf{R}_{+z}^2$	$4 - x \mathbf{I}$	$8 + y \mathbf{I}$	$6 - y \mathbf{I}$	$5 + z \mathbf{I}$	$5 - z \mathbf{I}$
6	$(0, 0, 0)$	$3 + x \mathbf{I}$	$3 - x \mathbf{I}$	$5 + y \mathbf{I}$	$7 - y \mathbf{I}$	$6 + z \mathbf{I}$	$6 - z \mathbf{I}$
7	$(0, L, 0)$	$5 - x \mathbf{R}_{-z}^2$	$2 - x \mathbf{I}$	$6 + y \mathbf{I}$	$8 - y \mathbf{I}$	$7 + z \mathbf{I}$	$7 - z \mathbf{I}$
8	$(0, 2L, 0)$	$1 + x \mathbf{I}$	$1 - x \mathbf{I}$	$7 + y \mathbf{I}$	$5 - y \mathbf{I}$	$8 + z \mathbf{I}$	$8 - z \mathbf{I}$

Acknowledgments

We thank James Isenberg for comments and suggestions that helped us improve the clarity of this article. F. Z. was supported by the National Natural Science Foundation of China grants 12073005, 12021003, 11503003 and 11633001, and the Interdiscipline Research Funds of Beijing Normal University. L. L. was supported in part by NSF grant 2012857 to the University of California at San Diego.

Data Availability

The authors will attempt to honor reasonable requests for the datasets generated and analyzed as part this study.

References

1. Cook G B 2000 *Living Reviews in Relativity* **3**(5), 53
2. Pfeiffer H P, Kidder L E, Scheel M A and Teukolsky S A 2003 *Comput. Phys. Commun.* **152** 253–273
3. OKAWA H 2013 *International Journal of Modern Physics A* **28** 1340016
4. Ossokine S, Foucart F, Pfeiffer H P, Boyle M and Szilágyi B 2015 *Classical and Quantum Gravity* **32** 245010
5. Tichy W, Rashti A, Dietrich T, Dudi R and Brüggmann B 2019 *Phys. Rev. D* **100** 124046
6. Lindblom L, Rinne O and Taylor N W 2022 *J. Comp. Math.* (in press)
7. Burton B A, Budney R, Pettersson W *et al.* 1999–2021 Regina: Software for low-dimensional topology <http://regina-normal.github.io/>
8. Yamabe H 1960 *Osaka J. Math.* **12** 21–37
9. Bartnik R and Isenberg J 2004 The constraint equations *The Einstein Equations and the Large Scale Behavior of Gravitational Fields* ed Crusciel P and Friedrich H (Springer) pp 1–38
10. Thurston W P 1997 *Three-Dimensional Geometry and Topology* (Princeton University Press)
11. Scott P 1983 *Bull. London Math. Soc.* **15** 401–487

-
12. Isenberg J 1995 *Classical and Quantum Gravity* **12** 2249–2274
 13. Lindblom L and Szilágyi B 2013 *J. Comput. Phys.* **243** 151-175
 14. Balay S, Abhyankar S, Adams M F, Benson S, Brown J, Brune P, Buschelman K, Constantinescu E, Dalcin L, Dener A, Eijkhout V, Gropp W D, Hapla V, Isaac T, Jolivet P, Karpeev D, Kaushik D, Knepley M G, Kong F, Kruger S, May D A, McInnes L C, Mills R T, Mitchell L, Munson T, Roman J E, Rupp K, Sanan P, Sarich J, Smith B F, Zampini S, Zhang H, Zhang H and Zhang J 2021 PETSc/TAO users manual Tech. Rep. ANL-21/39 - Revision 3.16 Argonne National Laboratory
 15. Lindblom L, Taylor N W and Rinne O 2016 *J. Comput. Phys.* **313** 31-56